Available online at www.sciencedirect.com
ScienceDirect
Trans. Nonferrous Met. Soc. China 25(2015) 783−790
Transactions of Nonferrous Metals Society of China
www.tnmsc.cn

Oxidation behavior of Zr-containing Ti_2AlNb-based alloy at 800 °C

Wei DANG, Jin-shan LI, Tie-bang ZHANG, Hong-chao KOU

State Key Laboratory of Solidification Processing, Northwestern Polytechnical University, Xi'an 710072, China

Received 5 June 2014; accepted 31 July 2014

Abstract: The oxidation behavior of Ti−22Al−(27−x)Nb−xZr (x=0, 1, 6) alloys at 800 °C for exposure time up to 100 h was examined. It is shown that oxidation rate of experimental alloys obeys the parabolic kinetics. Ti−22Al−26Nb−1Zr alloy demonstrates more excellent oxidation resistance than the other two alloys. The main oxidation products are TiO_2, Al_2O_3 and $AlNbO_4$ phases for all these alloys. For the Ti−22Al−26Nb−1Zr alloy, Zr addition can modify the growth mechanism of oxide scale, which can effectively hinder the diffusion of oxygen. Whereas, reaction of Zr with oxygen leads to the formation of ZrO_2 precipitates for the Ti−22Al−21Nb−6Zr alloy, which promotes the oxygen ingress into the substrate. Meanwhile, oxidation affected zones, including internal-oxidation layer and oxygen-enriched zone, are present beneath the outmost oxide scale. The difference in these zones is derived from the phase constitution in the starting Ti−22Al−(27−x)Nb−xZr (x=0, 1, 6) alloys.

Key words: oxidation behavior; Ti_2AlNb-based alloy; Zr; oxide scale; oxidation affected zone

1 Introduction

Ti_2AlNb-based alloys have received considerable attention after the first report on the orthorhombic phase with stoichiometric composition close to Ti_2AlNb in Ti−Al−Nb alloy system [1]. These alloys have great potential application in aircraft engines due to their acceptable combination of strength, toughness and ductility [2]. However, there are still limits for their application in structural components at elevated temperature because of unsatisfactory high-temperature oxidation resistance, especially above 700 °C [3,4]. According to some reports concerning the oxidation of Ti_2AlNb-based alloys at the temperature above 650 °C [5,6], oxidation products consist of an alumina-rich outer layer, which is not fully dense due to the presence of TiO_2 and $AlNbO_4$. In addition, oxygen and nitrogen contribute to subsurface brittleness because of interstitial solutes or formation of oxygen- and nitrogen-containing phases. Up to now, great progress such as protective coating has been made to improve oxidation resistance of Ti_2AlNb-based alloy [3,7]. However, poor binding force between oxidation resistant coatings and base alloys severely restricts their service during thermal cycling. As demonstrated, it is more effective and economical to provide high oxidation resistance by the addition of certain elements to the alloy [8−10]. Oxidation data of various Ti−Al−Nb alloys indicate that oxidation resistance can be improved by the addition of Nb through inhibiting mass transfer in TiO_2 [11,12], but further increase in Nb content deteriorates the oxidation resistance because of the formed $TiNb_2O_7$ or $AlNbO_4$ phases [6,13]. Meanwhile, when Nb and Al elements coexist, each of them can reduce the beneficial effect of the other on oxidation resistance [13]. For Ti_2AlNb-based alloys, oxidation resistance can be improved by higher Al/Nb ratio and Zr addition [14]. Additionally, it has been confirmed that the addition of Zr preserves beneficial effect on creep strength without deteriorating yield stress and RT elongation [14].

Taking these advantages of Zr addition and enhancement of Al/Nb ratio into consideration, the present work, based on the initial Ti−22Al−27Nb alloy, extends the range of composition and yields possible improvement of high temperature oxidation resistance to meet the requirements for advanced parts of modern jet engines. This work focuses on the oxidation behavior of Ti−22Al−(27−x)Nb−xZr (x=0, 1, 6) alloys, including phases of oxidation products, distribution of elements in the scale and morphology of subsurface zone. The oxidation behavior and corresponding mechanism are

Foundation item: Project (2011CB605503) supported by the National Basic Research Program of China
Corresponding author: Tie-bang ZHANG; Tel:+86-29-88491764; Fax: +86-29-88460294; E-mail: tiebangzhang@nwpu.edu.cn
DOI: 10.1016/S1003-6326(15)63664-0

proposed in order to provide a basis for the further development and better design of novel Ti_2AlNb-based alloys with promising oxidation resistance.

2 Experimental

Nominal compositions of the test alloys were Ti−22Al−27Nb, Ti−22Al−26Nb−1Zr and Ti−22Al−21Nb−6Zr (mole fraction, %). These alloys were melted by vacuum consumable electrode melting three times to ensure the chemical homogeneity. The ingots were then broken down in β/*B*2 field, followed by an extra β/*B*2 forging plus a subtransus low temperature forging. The alloys were solution-treated at 1080 °C for 1 h, water-quenched, aged at 830 °C for 4 h, and then water-quenched. Phase structural analysis was performed by X-ray diffraction (XRD) with Cu K_α radiation. The microstructure of the specimens was characterized by scanning electron microscopy (SEM).

Testing specimens with nominal dimensions of 10 mm×10 mm×4 mm were cut by electro spark erosion. Specimen surfaces were subsequently ground down to 1500 grit surface finish and finally ultrasonically cleaned in ethanol. Oxidation tests were carried out in laboratory at 800 °C for 100 h. During the testing process, specimens were placed in alumina crucibles, oxidized at the mentioned temperature, and removed from furnace at regular time intervals for mass measurements.

The mass of specimens before and after oxidation was measured using an analytic balance with an accuracy of 0.1 mg to characterize oxidation kinetics. Subsequently, phase identification of the oxides in the scales was performed by XRD. Surface and cross-sectional morphologies of the specimens were examined by SEM. The corresponding elemental profiles in cross-section were analyzed by energy dispersive spectroscopy (EDS) and electron probe micro analysis (EPMA). Cross-sectional microhardness was tested using a Vickers hardness instrument at a load of 25 g with a dwell time of 10 s.

3 Results and discussion

3.1 Phase constitution of starting materials

Figure 1 shows XRD patterns obtained from Ti−22Al−27Nb, Ti−22Al−26Nb−1Zr and Ti−22Al−21Nb−6Zr alloys after solution and aging. All the samples show diffraction peaks for crystallographic *B*2 (ordered BCC phase), BCC and *O* phases. For identification of *B*2 phase, its (100) peak should be observed. In Figs. 1(a) and (b), it is uncertain that (100) peak of *B*2 phase and (111) peak of *O* phase strongly overlap or reflection of (100) is too weak to be detected. But in Fig. 1(c), Bragg peaks of the super-lattice *B*2 phase are obvious.

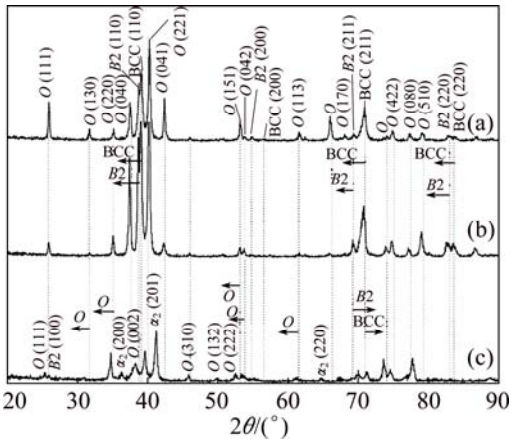

Fig. 1 XRD patterns of Ti−22Al−(27−*x*)Nb−*x*Zr alloys used for isothermal oxidation experiments: (a) *x*=0; (b) *x*=1; (c) *x*=6

Based on the phase diagram and reports for Ti−22Al−*x*Nb [15,16], it is reasonable to consider that the disordered BCC phase and ordered *B*2 phase might co-exist in these test alloys. Particularly, for Ti−22Al−21Nb−6Zr, Bragg peaks belonging to α_2 phase are also detected, but peaks of BCC phases are relatively weak, because the precipitation of α_2 phase leads to the sufficiency of Al in *B*2 phase. Transformation of *B*2 phase to BCC is derived by the Al depleted in *B*2 phase [15]. On careful comparison between Ti−22Al−27Nb and Zr-containing alloys, it is noted that there is relative shift of intensity peaks for *O*, *B*2 and BCC phases, as shown by dotted lines in Fig. 1. Peaks of *O*, *B*2 and BCC phases in Ti−22Al−26Nb−1Zr alloy seem to be shifted toward lower 2θ angle, indicating that interplanar spacing of Zr-containing *B*2, BCC and *O* phases might be larger than that of phase without Zr. The variance of lattice parameters is greater for Ti−22Al−21Nb−6Zr compared with Ti−22Al−26Nb−1Zr, as indicated in Table 1. Considering the atomic radius, covalent radius and electronegativity, the effect of these elements on unit-cell size can be sorted as Zr, Nb, Ti and Al in descending order. And it is confirmed that Zr element can increase the lattice parameters of β phase [17]. However, Ti−22Al−21Nb−6Zr alloy exhibits lower volume fractions of *B*2 and BCC phases containing a greater Al content due to the precipitation of α_2 phase. In addition, the decrease in Nb content in *B*2 phase could arise from less Nb in this alloy. This synergistic effect of Al and Nb reduces lattice parameters of BCC and *B*2 phases, and thus the corresponding peaks shift to higher 2θ value.

3.2 Oxidation kinetics

The average mass gains for Ti−22Al−27Nb, Ti−22Al−26Nb−1Zr and Ti−22Al−21Nb−6Zr alloys, as shown in Fig. 2(a), are 1.28, 0.95 and 1.56 mg/cm^2,

Table 1 Identified phases and corresponding crystallographic parameters for Ti−22Al−(27−*x*)Nb−*x*Zr (*x*=0, 1, 6) alloys

Ti−22Al−(27−*x*)Nb−*x*Zr	Phase	*a*/Å	*b*/Å	*c*/Å
x=0	BCC/*B*2	3.2622	3.2622	3.2622
	O	3.3136	3.3136	3.3136
	α_2	5.9788	9.5972	4.6607
		–	–	–
x=1	BCC/*B*2	3.2642	3.2642	3.2642
	O	3.3036	3.3036	3.3036
	α_2	5.9838	9.5828	4.6720
		–	–	–
x=6	BCC/*B*2	3.2446	3.2446	3.2446
	O	3.2915	3.2915	3.2915
	α_2	6.0634	9.8993	4.7551
		5.7274	5.7274	4.6999

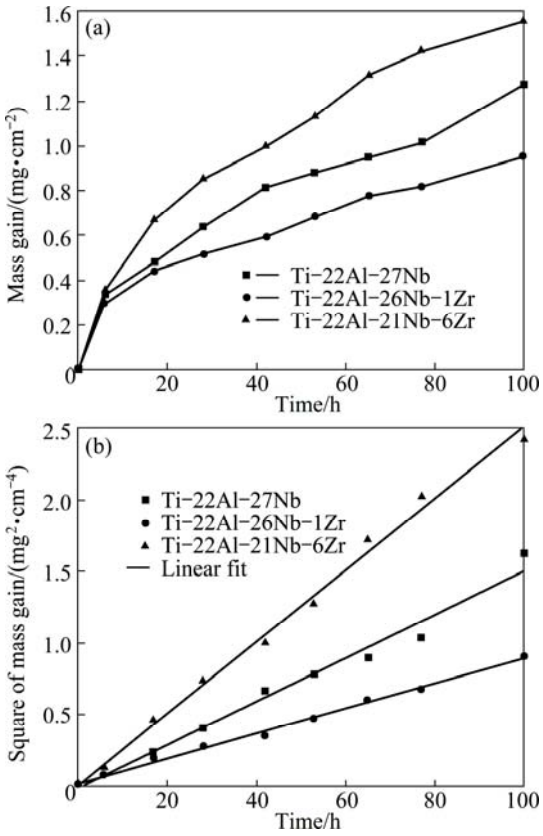

Fig. 2 Mass gain (a) and square of mass gain (b) versus time of Ti−22Al−(27−*x*)Nb−*x*Zr (*x*=0, 1, 6) alloys during oxidation at 800 °C in air

respectively. The general oxidation behavior of all the alloys is quite similar in the whole oxidation process. However, Ti−22Al−26Nb−1Zr alloy demonstrates more excellent oxidation resistance than the other two alloys. The curves of square of mass gain versus time are plotted for the comparison of oxidation rate constants, as shown in Fig. 2(b). Ti−22Al−26Nb−1Zr alloy exhibits the lowest oxidation rate constant (k_p), 8.0×10^{-3} mg^2/(cm^4·h), which can be determined by the slope of linear fit [18].

Oxidation data of these three alloys and other Ti−Al−Nb alloys with 22% Al and 25% Al (mole fraction) are plotted in Fig. 3. Literature data were obtained from Refs. [5,6,19,20]. The investigation about the effect of Nb additions on oxidation behavior of Ti−25Al alloys has shown that oxidation resistance can be improved at Nb levels up to the critical value. With the same content of Nb, Ti−22Al alloy has higher k_p value than Ti−25Al, and higher Al/Nb ratio leads to the improvement in oxidation resistance. In order to evaluate the effect of Zr on oxidation resistance without interference with Nb, comparison of the present three alloys with Ti−22Al−*x*Nb alloys shows that the oxidation resistance of Ti−22Al−21Nb−6Zr alloy is inferior, and Ti−22Al−26Nb−1Zr alloy is better than that of the alloys without Zr.

3.3 Phase compositions and morphologies of oxide scales

Figure 4 shows XRD patterns of the oxide layers formed on the surface of Ti−22Al−27(Nb,Zr) specimens

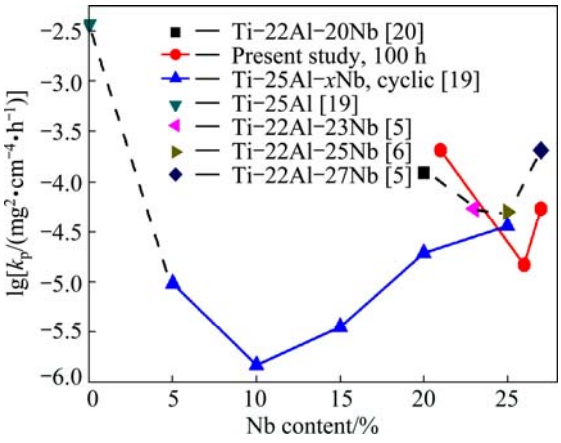

Fig. 3 Parabolic rate constant vs Nb content for various Ti−22Al and Ti−25Al alloys

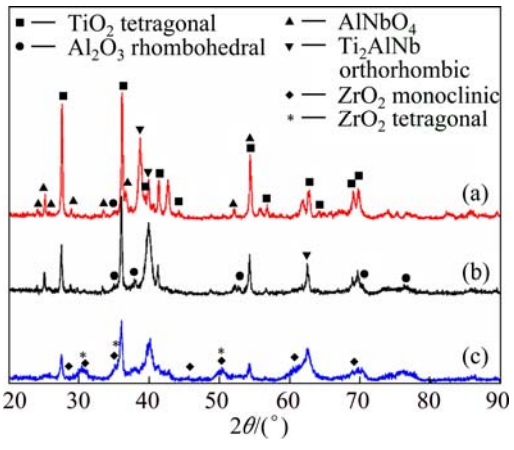

Fig. 4 Scale surface XRD patterns of Ti−22Al−(27−*x*)Nb−*x*Zr alloys after oxidation at 800 °C for 100 h: (a) *x*=0; (b) *x*=1; (c) *x*=6

during holding at 800 °C for 100 h. Bragg peaks of TiO_2, $AlNbO_4$ and Al_2O_3 phases are all detected in these three alloy. For Ti−22Al−26Nb−1Zr alloy, the intensity of Al_2O_3 peaks increases, which indicates the existence of more Al_2O_3 product. However, for Ti−22Al−21Nb−6Zr alloy, in addition to several Bragg peaks of $AlNbO_4$, intensity of Bragg peaks from monoclinic- and tetragonal-ZrO_2 grows up.

Figure 5(a) shows XRD patterns of Ti−22Al−26Nb−1Zr alloy oxidized at 800 °C for different time. It can be seen that the peaks of Al_2O_3 and TiO_2 can be observed for the alloy oxidized at 800 °C for 6 h. In addition, the intensity of TiO_2 peaks increases and diffraction patterns of $AlNbO_4$ appear at 42 h. The intensity of $AlNbO_4$ peaks increases obviously with oxidation from 42 h to 100 h. Figure 5(b) shows scale surface XRD patterns of Ti−22Al−21Nb−6Zr alloys oxidized at 800 °C for different time. Compared with Fig. 5(a), additional peaks of ZrO_2 with very weak intensity appear at 6 h. With the increase in oxidation time, the intensity of TiO_2 and Al_2O_3 peaks is obviously enhanced for Ti−22Al−21Nb−6Zr alloy. And after oxidation at 800 °C for 100 h, the Bragg peaks from monoclinic- and tetragonal-ZrO_2 increase. The oxidation products are found to be mainly TiO_2, Al_2O_3 and ZrO_2 with a little amount of $AlNbO_4$.

The surface morphologies formed on the Ti−22Al−27(Nb,Zr) samples oxidized at 800 °C are displayed in Fig. 6. The oxides are inclined to evolve and link up along the flats between every two grinding marks caused by specimen preparation, as stress relaxation of oxide growth occurs at the edges of each grinding mark. In Fig. 6(a), TiO_2 nodules form and grains in these nodules grow and link up as islands, consuming Ti from the surroundings. But the surface of alloy is covered by a thin discontinuous layer due to the joints among different islands. The formation of this layer leads to a local enrichment of Al. So, beneath this layer, the fine-grained Al_2O_3 and TiO_2 form (fine-grained TiO_2/Al_2O_3). Compared with Ti−22Al−27Nb alloy, as can be seen from Figs. 6(b) and (c), a rather compact oxide layer exists which is derived from the combination of fewer TiO_2 nodules and much more fine-grained

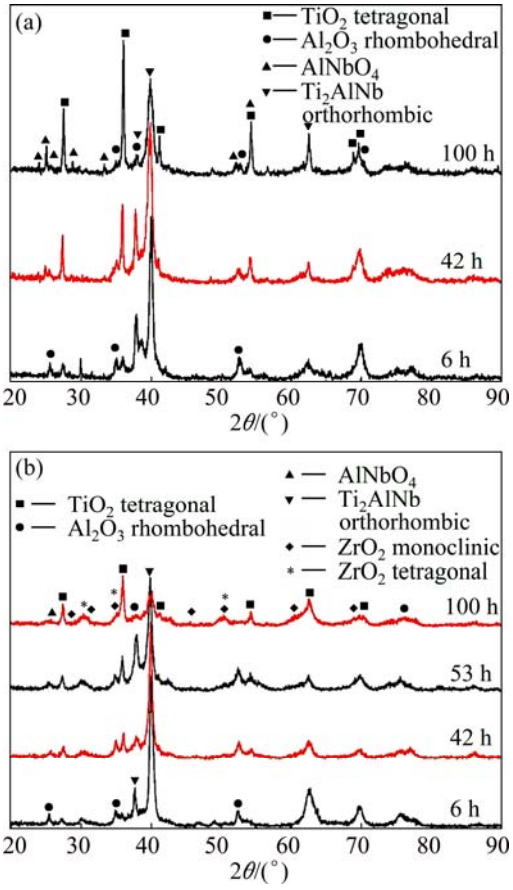

Fig. 5 XRD patterns of specimens oxidized at 800 °C in air for different time: (a) Ti−22Al−26Nb−1Zr; (b) Ti−22Al−21Nb−6Zr

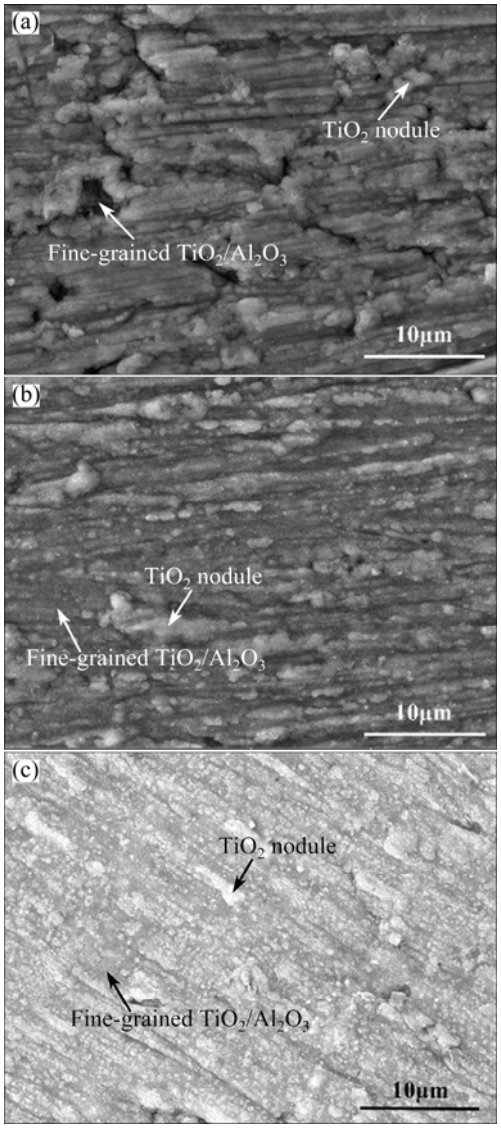

Fig. 6 Surface morphologies of Ti−22Al−(27−*x*)Nb−*x*Zr alloys after oxidation at 800 °C for 100 h: (a) *x*=0; (b) *x*=1; (c) *x*=6

TiO_2/Al_2O_3 are formed on the surface of oxide layer in Ti−22Al−21Nb−6Zr alloy.

3.4 Cross-sectional analysis

Figure 7 presents cross-sectional morphologies and corresponding element profiles. The oxide scale for Ti−22Al−26Nb−1Zr alloy is the thinnest, only about 2 μm. A layer with thickness of about 8 μm is formed for Ti−22Al−21Nb−6Zr alloy. These results are in accordance with the mass gain after oxidation. Compared with Fig. 7(c), oxide layer is delaminated as two parts obviously in Figs. 7(a) and (e). This reveals that the interface bonding is relatively firm between different layers in Ti−22Al−26Nb−1Zr alloy. In addition, for

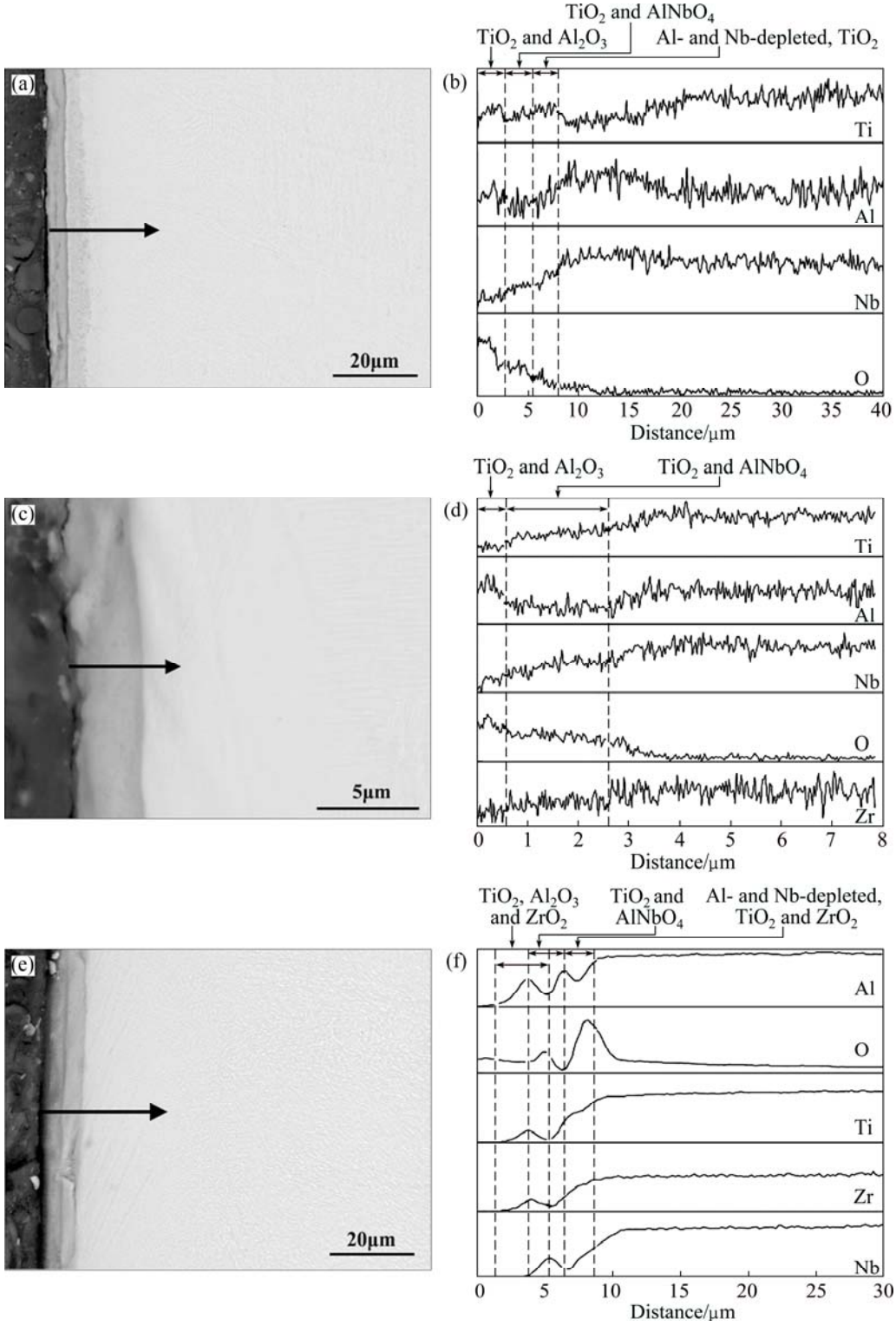

Fig. 7 Cross-sectional morphologies (a, c, e) and corresponding elemental profiles (b, d, f) in Ti−22Al−(27−*x*)Nb−*x*Zr alloys oxidized at 800 °C for 100 h: (a, b) *x*=0; (c, d) *x*=1; (e, f) *x*=6

Ti−22Al−21Nb−6Zr alloy, partial oxide layer separates from the surface of alloy.

Based on the above XRD analysis and comparing the variety of Ti, Al, Nb and O elements in cross sections, as shown in Fig. 7(b), it is concluded that oxide scales of Ti−22Al−27Nb alloy, from surface to base alloy, are outer Al_2O_3 and TiO_2 layer, intermediate layer containing both TiO_2 and $AlNbO_4$, and inner TiO_2 layer. As shown in Fig. 7(d), the external layer mostly contains TiO_2 and Al_2O_3, while the internal one is a mixture of TiO_2 and $AlNbO_4$ in Ti−22Al−26Nb−1Zr alloy. Compared with Fig. 7(b), the intensity of Al in the external layer is much higher for Ti−22Al−26Nb−1Zr alloy, indicating that Zr addition increases the formation of Al_2O_3. As can be seen from Fig. 7(f), the oxide scale of Ti−22Al−21Nb−6Zr alloy consists of outer ZrO_2, TiO_2 and Al_2O_3 mixture layer, intermediate $AlNbO_4$ layer, and inner layer containing some TiO_2 and ZrO_2. Additionally, a transition region exists between outer and intermediate layers. Initially formed loose oxide scale facilitates inward diffusion of oxygen and formation of large amount of TiO_2 and ZrO_2, together with the generation of $AlNbO_4$ in the Al-rich region. Minor Zr solution in this Al-rich region accelerates the formation of Al_2O_3 in this transition region.

Combined with the information from the element profiles, the high oxygen content in the substrates results in delamination in Fig. 7(e). Plasticity of alloys decreases with the solubility of oxygen into the substrates, which results in some difficulties about the release of the internal stress in oxide film by plastic deformation near the layer/metal interface [21]. Pilling-bedworth ratio (PBR) for Zr/ZrO_2 is 1.56, which indicates that large compressive stress is generated in the oxide layer [22]. This stress could induce cracking and swelling. Compared with the outmost ZrO_2 formed on free surface, at the interface between the layer and matrix, ZrO_2 can contribute to internal stress greatly.

According to the above oxidation process, the morphology of initially formed Al_2O_3 scales, which has significant effect on the inward diffusion rate of oxygen, plays an important role in the oxidation behavior of the alloys. For the alloys with addition of Zr, a large amount of Al_2O_3 scales can be demonstrated by the results of XRD patterns in Ti−22Al−27Nb−1Zr and Ti−22Al−21Nb−6Zr alloys oxidized at 800 °C for 6 h (Fig. 6). According to previous research results [23,24], a certain amount of Zr can accelerate the nucleation of Al_2O_3 grains and modify the growth mechanism of Al_2O_3 scales, correspondingly hindering the diffusion of oxygen through the scales. But further increase in Zr content to 6% (mole fraction) results in the formation of ZrO_2. ZrO_2 incorporated in the oxide scale is a metal-excess n-type oxide with anion vacancies, providing sites for rapid oxygen transport [22].

With further ingress for oxygen, oxidation affected zones are present beneath the external oxide scale mentioned above. These zones have higher hardness than the bulk alloys up to a certain depth of some microns. The Ti_2AlNb-based alloys present microstructures with *O* and BCC/*B*2 phase, or containing α_2 phase. BECKER et al [25] have reported that the largest solubility of oxygen in α_2 phase is about 20%, while BCC/*B*2 phase can dissolve minimum but with a highest diffusivity. The cross-sectional microhardness profile shows that oxygen permeates into the alloy up to a depth of around 80 μm for Ti−22Al−21Nb−6Zr alloy. It should be noted that in Ti−22Al−27Nb sample relatively thin oxidation affected zones are observed. The zones consist of two distinct layers as etched by acid, as shown in Fig. 8. Layer I, internal-oxidation layer, reveals a complex microstructure. For γ-TiAl-based alloys, the internal-oxidation layer is an Al-depleted layer, consisting of a

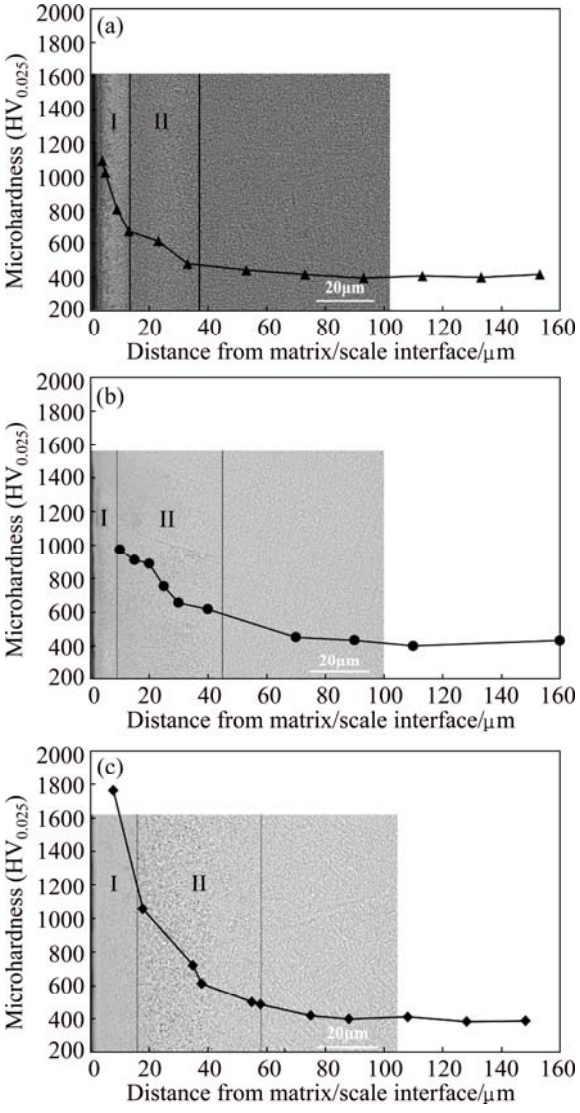

Fig. 8 Microhardness and SEM images of cross-section for Ti−22Al−(27−*x*)Nb−*x*Zr alloys: (a) *x*=0; (b) *x*=1; (c) *x*=6

cubic Z-$Ti_5Al_3O_2$ and oxygen-enriched α_2 phases [26−28]. Whereas, for α_2-Ti_3Al, oxygen- and Al-enriched α-Ti, α-Al_2O_3 and ternary Ti−21Al−15O phases are in this layer [29]. However, in Ti_2AlNb-based alloy, TiO_x or $(Ti, Nb)_xO$ is identified and precipitates in BCC phase [29]. Because the diffusion rate of oxygen in BCC β phase is the highest, oxygen should rapidly penetrate β-(Ti, Nb), and TiO_x could form once the solubility limit of oxygen is exceeded [30]. For Ti−22Al−26Nb−1Zr alloy, the thickness of layer I is the thinnest. Besides role of the external oxide layer in hindering oxygen ingress, the intervals between different lattice points in Ti−22Al−26Nb−1Zr alloy are larger, resulting in stronger ability to dissolve and more diffusion paths for oxygen than Ti−22Al−27Nb alloy, so oxygen could diffuse inwards without even more formation of TiO_x or $(Ti,Nb)_xO$. On the contrary, the decrease in lattice parameter of $B2$ phase together with absorption and solution of oxygen preferentially in α_2 phase, determines the feature of internal-oxidation layer in Ti−22Al−21Nb−6Zr alloy.

As oxygen diffuses inward further, reduction in oxygen partial pressure leads to the dissolution and diffusion of oxygen in layer II, the oxygen-enriched zone. In Ti−22Al−26Nb−1Zr alloy, this zone is wider than that of Ti−22Al−27Nb alloy, as the capability of dissolution and diffusion is enhanced for the phases with Zr addition. In addition, for Ti−22Al−21Nb−6Zr alloy, the presence of α_2 phase with the largest solubility is one major reason for the largest oxygen-enriched zone, and the highest lattice parameter of O phase is conducive to diffusive mass transfer.

4 Conclusions

1) Oxidation rates of Ti−22Al−(27−x)Nb−xZr (x=0, 1,6) alloys obey parabolic kinetics after oxidation at 800 °C for exposure time up to 100 h. Ti−22Al−26Nb−1Zr alloy demonstrates more excellent oxidation resistance than the other two alloys.

2) Oxide scale is varied with Zr addition. In Ti−22Al−26Nb−1Zr alloy, Zr addition can modify the growth mechanism of oxidation scale, hindering the diffusion of oxygen. Whereas, the reaction of 6% Zr with oxygen leads to the formation of tetragonal- and monoclinic-ZrO_2 precipitates, which promotes the oxygen ingress into the substrate.

3) The starting phase and microstructure of the alloys are altered by Zr addition, resulting in different degrees of oxygen affected zones. For Ti−22Al−26Nb−1Zr alloy, the stronger ability to dissolve and more diffusion paths for oxygen due to larger lattice parameters of BCC/$B2$ and O phases lead to the thinnest internal-oxidation layer, while for Ti−22Al−21Nb−6Zr alloy, the oxygen dissolves into substrate easily due to the presence of α_2 phase and enhancement of lattice parameter for O phase with 6% Zr addition.

References

[1] BANERJEE D, GOGIA A K, NANDI T K, JOSHI V A. A new ordered orthorhombic phase in a Ti_3Al−Nb alloy [J]. Acta Metallurgica, 1988, 36(4): 871−882.

[2] XUE C, ZENG W, WANG W, LIANG X, ZHANG J. Quantitative analysis on microstructure evolution and tensile property for the isothermally forged Ti_2AlNb based alloy during heat treatment [J]. Materials Science and Engineering A, 2013, 573: 183−189.

[3] KONG L, QI J, LU B, YANG R, CUI X, LI T, XIONG T. Oxidation resistance of $TiAl_3$−Al composite coating on orthorhombic Ti_2AlNb based alloy [J]. Surface and Coatings Technology, 2010, 204(14): 2262−2267.

[4] WU H Y, ZHANG P Z, ZHAO H F, WANG L, XIE A G. Effect of different alloyed layers on the high temperature oxidation behavior of newly developed Ti_2AlNb-based alloys [J]. Applied Surface Science, 2011, 257(6): 1835−1839.

[5] LEYENS C. Oxidation of orthorhombic titanium aluminide Ti−22Al−25Nb in air between 650 and 1000 °C [J]. Journal of Materials Engineering and Performance, 2001, 10(2): 225−230.

[6] LEYENS C, GEDANITZ H. Long-term oxidation of orthorhombic alloy Ti−22Al−25Nb in air between 650 and 800 °C [J]. Scripta Materialia, 1999, 41(8): 901−906.

[7] WANG Y H, LIU Z G, OUYANG J H, WANG Y M, ZHOU Y. Preparation and high temperature oxidation resistance of microarc oxidation ceramic coatings formed on Ti_2AlNb alloy [J]. Applied Surface Science, 2012, 258(22): 8946−8952.

[8] JIANG Hui-yen, WANG Zhong-lei, MA Wen-shuai, FENG Xiao-ran, DONG Zi-qiang, ZHANG Liang, LIU Yong. Effects of Nb and Si on high temperature oxidation of TiAl [J]. Transactions of Nonferrous Metals Society of China, 2008, 18(3): 512−517.

[9] POPELA T, VOJTĚCH D, VOGT J B, MICHALCOV A. Structural, mechanical and oxidation characteristics of siliconized Ti−Al−X (X=Nb, Ta) alloys [J]. Applied Surface Science, 2014, 307: 579−588.

[10] PILONE D, FELLI F, BROTZU A. High temperature oxidation behaviour of TiAl−Cr−Nb−Mo alloys [J]. Intermetallics, 2013, 43: 131−137.

[11] LIN J P, ZHAO L L, LI G Y, ZHANG L Q, SONG X P, YE F, CHEN G L. Effect of Nb on oxidation behavior of high Nb containing TiAl alloys [J]. Intermetallics, 2011, 19(2): 131−136.

[12] QIAN Yu-hai, LI Mei-shuan, LU Bin. Isothermal oxidation behavior of Ti_3Al-based alloy at 700−1000 °C in air [J]. Transactions of Nonferrous Metals Society of China, 2009, 19(3): 525−529.

[13] JIANG H, HIROHASI M, LU Y, IMANARI H. Effect of Nb on the high temperature oxidation of Ti−(0−50 at.%)Al [J]. Scripta Materialia, 2002, 46(9): 639−643.

[14] GERMANN L, BANERJEE D, GUEDOU J, STRUDEL J L. Effect of composition on the mechanical properties of newly developed Ti_2AlNb-based titanium aluminide [J]. Intermetallics, 2005, 13(9): 920−924.

[15] BOEHLERT C, MAJUMDAR B, SEETHARAMAN V, MIRACLE D. The microstructural evolution in Ti−Al−Nb O+BCC orthorhombic alloys [J]. Metallurgical and Materials Transactions A, 1999, 30(9): 2305−2323.

[16] WANG W, ZENG W, XUE C, LIANG X, ZHANG J. Quantitative analysis of the effect of heat treatment on microstructural evolution and microhardness of an isothermally forged Ti−22Al−25Nb (at.%) orthorhombic alloy [J]. Intermetallics, 2014, 45: 29−37.

[17] DAI Shi-juan, WANG Yu, CHEN Feng, YU Xin-quan, ZHANG You-fa. Influence of Zr content on microstructure and mechanical properties of implant Ti−35Nb−4Sn−6Mo−*x*Zr alloys [J]. Transactions of Nonferrous Metals Society of China, 2013, 23(5): 1299−1303.

[18] CHENG Yang, ZHANG Heng, SONG Li-wen, MA Yue, LI Shu-suo, GONG Shang-kai. Effect of Re element on oxidation resistance of Ni_3Al−Mo based alloys at 1150 °C [J]. Transactions of Nonferrous Metals Society of China, 2012, 22(3): 510−515.

[19] GAUER L, ALPERINE S, STEINMETZ P, VASSEL A. Influence of niobium additions on high-temperature-oxidation behavior of Ti_3Al alloys and coatings [J]. Oxidation of Metals, 1994, 42(1−2): 49−74.

[20] JHA S, KHANNA A, HARENDRANATH C. High temperature oxidation behaviour of Ti_3Al−Nb intermetallics [J]. Materials Science Forum, 1997, 251: 203−210.

[21] AKHIANI H, SZPUNAR J A. Effect of surface roughness on the texture and oxidation behavior of zircaloy-4 cladding tube [J]. Applied Surface Science, 2013, 285: 832−839.

[22] XIE X, ZHANG J, YAO M, ZHOU B, PENG J, LIANG X. Oxide microstructural evolution of Zr−0.7Sn−0.35Nb−0.3Fe alloys containing Ge corroded in lithiated water [J]. Journal of Nuclear Materials, 2014, 451(1−3): 255−263.

[23] LE GALL M, HUNTZ A, LESAGE B, MONTY C, BERNARDINI J. Self-diffusion in α-Al_2O_3 and growth rate of alumina scales formed by oxidation: Effect of Y_2O_3 doping [J]. Journal of Materials Science, 1995, 30(1): 201−211.

[24] TANIGUCHI S, JUSO H, SHIBATA T. Improvement in high-temperature oxidation resistance of TiAl by addition of 0.2 mass% Zr [J]. Materials Transactions—JIM, 1996, 37: 245−251.

[25] BECKER S, RAHMEL A, SCHORR M, SCH TZE M. Mechanism of isothermal oxidation of the intermetallic TiAl and of TiAl alloys [J]. Oxidation of Metals, 1992, 38(5−6): 425−464.

[26] BRAUN R, KELM K, FRHLICH M, LEYENS C. Oxidation resistance of γ-TiAl based alloy Ti−45Al−8Nb coated with intermetallic Ti−Al−Cr−Y layers and EB-PVD zirconia topcoats at 950 °C in air [J]. Surface and Coatings Technology, 2013, 222: 128−134.

[27] LI W, ZHU S, CHEN M, WANG C, WANG F. Development of an oxidation resistant glass–ceramic composite coating on Ti−47Al−2Cr−2Nb alloy [J]. Applied Surface Science, 2014, 292: 583−590.

[28] COPLAND E H, GLEESON B, YOUNG D J. Formation of *Z*-$Ti_{50}Al_{30}O_{20}$ in the sub-oxide zones of gamma-TiAl-based alloys during oxidation at 1000 °C [J]. Acta Materialia, 1999, 47(10): 2937−2949.

[29] DETTENWANGER F, SCHUTZE M. Isothermal oxidation of α_2-Ti_3Al [J]. Oxidation of Metals, 2000, 54(1−2): 121−138.

[30] CERCHIARA R R. The oxidation and embrittlement of orthorhombic *O*-Ti_2AlNb based system [D]. Ann Arbor: University of Pittsburgh, 1996: 123−125.

含锆 Ti_2AlNb 基合金在 800 °C 的高温氧化行为

党 薇，李金山，张铁邦，寇宏超

西北工业大学 凝固技术国家重点实验室，西安 710072

摘　要：研究 Ti−22Al−(27−*x*)Nb−*x*Zr (*x*=0，1，6)合金在 800 °C 暴露时间长达 100 h 条件下的氧化行为。结果表明，合金氧化速率符合抛物线规律。Ti−22Al−26Nb−1Zr 合金的氧化性能优于其他两种合金。这些合金的氧化产物主要有 TiO_2、Al_2O_3 和 $AlNbO_4$。对于 Ti−22Al−26Nb−1Zr 合金，Zr 的添加可以改善氧化层的生长过程，从而有效阻止氧的扩散。然而，对于 Ti−22Al−21Nb−6Zr 合金，Zr 与氧发生反应，形成 ZrO_2，ZrO_2 促使氧向合金基体内部扩散。同时，在氧化层下，存在包括内氧化层和富氧层的氧影响区域。不同合金氧影响区的差异主要归因于合金的初始相结构。

关键词：氧化行为；Ti_2AlNb 合金；锆元素；氧化层；氧影响区

(Edited by Wei-ping CHEN)